Construction and Building Materials 191 (2018) 564–574

Contents lists available at ScienceDirect

Construction and Building Materials

journal homepage: www.elsevier.com/locate/conbuildmat

Effects of Na_2O/SiO_2 molar ratio on properties of aggregate-paste interphase in fly ash-based geopolymer mixtures through multiscale measurements

Mahdieh Khedmati [a], Hani Alanazi [a], Yong-Rak Kim [b,*], Gabriel Nsengiyumva [a], Sussan Moussavi [a]

[a] *Department of Civil Engineering, University of Nebraska-Lincoln, United States*
[b] *Department of Civil Engineering, 362N Whittier Research Center, University of Nebraska-Lincoln, NE 68583-0856, United States*

HIGHLIGHTS

- The effects of Na_2O/SiO_2 molar ratio on the interphase of geopolymer was studied.
- The interphase presents more N-A-S-H gel than adjacent paste regardless of the Na_2O/SiO_2 ratios (0.8 and 1.6) attempted.
- The higher Na_2O/SiO_2 ratio led to increased interphase bonding between aggregate and paste.
- Mechanical and microstructural characteristics in different length scales were in good agreement.

ARTICLE INFO

Article history:
Received 5 June 2018
Received in revised form 24 September 2018
Accepted 4 October 2018

Keywords:
Fly ash-based geopolymer
Interphase
Nanomechanical properties
Microstructure
Multiscale
Na_2O/SiO_2 molar ratio

ABSTRACT

This paper presents a multiscale experimental study on the influence of different Na_2O/SiO_2 molar ratios on the mechanical and microstructural characteristics of the aggregate-paste interphase in fly ash-based geopolymer mixtures. By analyzing the scanning electron microscope images, the solid phases present in the microstructure were identified, and the frequency of occurrence of each phase was quantified. In addition, the porosity and pore size distribution of geopolymer specimens were measured by mercury intrusion porosimetry. By conducting nanoindentation tests on a large array of indentations and subsequent statistical analysis of the test results, the elastic moduli of individual phases were extracted. The bond behavior between aggregate and paste was also investigated by conducting the three-point bending test of single edge notched beam specimens. Integration of test results in different length scales showed that interphase region generates more sodium aluminosilicate hydrate (i.e., N-A-S-H) gel than the adjacent paste region regardless of the Na_2O/SiO_2 ratios used in this study. In addition, the mixture prepared with the higher Na_2O/SiO_2 molar ratio exhibited more N-A-S-H gel in the interphase zone, which led to increased bonding strength between aggregate and paste.

1. Introduction

Interphases in composite materials often play an important role of the whole composite behavior. The most important interphase in ordinary Portland cement (OPC) concrete is the interfacial transition zone (ITZ) which is typically defined as the zone between cement paste and aggregate [1]. The ITZ forms around each aggregate particle with a thickness usually of about 50 μm due to several phenomena such as the so called "wall-effect" where there is less calcium-silicate-hydrate (C-S-H), high porosity, a greater concentration of calcium hydroxide (CH), and ettringite [2,3]. It is believed that a higher difference in strength between the ITZs and surrounding phase leads to more micro-cracking in the ITZs [4,5]. Moreover, the higher porosity of the ITZs can significantly reduce the mechanical properties and durability of entire concrete by allowing easier penetration of aggressive species into concrete [6]. The importance of the ITZ in concrete comes from it being the weakest zone in the whole composite. Thus, the overall composite performance is strongly based on this single zone [7].

An alternative cementitious material that has obtained increasing attention in the field of civil engineering is fly ash-based geopolymer due to its low CO_2 emission without compromising mechanical properties. In geopolymerization technology, a variety

---

* Corresponding author.
E-mail addresses: mahdieh.khedmati@huskers.unl.edu (M. Khedmati), hani.alanazi@huskers.unl.edu (H. Alanazi), yong-rak.kim@unl.edu (Y.-R. Kim), gabriron01@huskers.unl.edu (G. Nsengiyumva), smoussavi@huskers.unl.edu (S. Moussavi).

https://doi.org/10.1016/j.conbuildmat.2018.10.024
0950-0618/© 2018 Elsevier Ltd. All rights reserved.

of by-products that are rich in silica and alumina such as fly ash and slag can be transformed into useful binding materials. Fly ash is an appropriate material to be used as a solid precursor to make geopolymers due to its chemical composition, low water demand, and worldwide availability [8]. The geopolymerization process consists of dissolution of the geopolymer reactants in a strong alkali solution such as sodium hydroxide and sodium silicate [9]. A polycondensation process leads to the formation of amorphous to semicrystalline polymers such as siloxo (—Si—O—Si—O—), sialate (—Si—O—Al—O—), sialate - siloxo (—Si—O—Al—O—Si—O—), and sialate-disiloxo (—Si—O—Al—O—Si—O—Si—O—) [10]. In geopolymers, the amorphous sodium aluminosilicate hydrate (so-called N-A-S-H) gel is the main reaction product of low calcium fly ash and is mainly responsible for strength development [11]. N-A-S-H has a similar elastic modulus to low density C-S-H, which is the main reaction product in OPC concrete through hydration [12–15]. Many studies have shown the feasibility of geopolymer concrete to supplement OPC concrete with sufficient durability and mechanical properties [16–18]. The microstructure and mechanical properties of geopolymer material have been evaluated in detail by several studies [19–22]. Findings from previous studies showed that a combination of sodium hydroxide with sodium silicate would improve the geopolymerization process greater than using sodium hydroxide alone [23–27]. Phoo-ngernkham et al. [28] studied the flexural strength of notched Portland cement concrete beams filled with alkali-activated binders using a three-point bending test. Their results showed that a combination of sodium hydroxide mixed with sodium silicate solution provided higher flexural strength of notched OPC beam than those of sodium hydroxide or sodium silicate alone. Previous studies have also observed that the Na_2O/SiO_2 molar ratio plays an important role in morphological, microstructural, and mechanical properties of fly ash-based geopolymers [29–36]. For instance, Silva de Vergas et al. [37] reported that geopolymer mortars made with higher Na_2O/SiO_2 molar ratio showed more compressive strength and denser morphology.

Despite the importance of the interphase region between aggregate and paste and its influence on the overall properties of the concrete mixtures, only a very limited number of studies have investigated the properties and characteristics of the interphase region in geopolymer concrete [38,39]. Furthermore, the influence of the Na_2O/SiO_2 molar ratio on the properties of the interphase region still leaves many questions and requires more observations. With the use of advanced microstructural and nanomechanical technologies, the interphase region in geopolymeric mixture can be properly characterized. In particular, nanoindentation is capable of assessing the mechanical properties of the individual constituents of cementitious materials quantitatively [20], and scanning electron microscope (SEM) aided by the energy dispersive X-ray spectroscopy (EDS) can identify the microstructural and chemical gradients of the interphase compared to the paste further from the aggregate [15,40,41].

This study aims to investigate the effects of different Na_2O/SiO_2 molar ratios on the microstructural characteristics, nanomechanical properties, and chemical aspects of fly ash-based geopolymer concrete by focusing on the interphase region. This is to better understand the differences in geopolymerization products resulting from different ratios of alkaline activators. Towards the end of the experimentation, SEM-EDS and nanoindentation tests were conducted to examine the small-scale interphase in geopolymer concretes designed in two different Na_2O/SiO_2 molar ratios. The aggregate-paste bond behavior was also investigated by employing a three-point bending test of single edge notched beam (SENB) specimens. In addition, the pore structure of the geopolymer pastes was characterized using mercury intrusion porosimetry (MIP) to examine the effect of different molar ratios of Na_2O/SiO_2 on the mixture's pore structure.

2. Materials and sample preparation

2.1. Materials and mixture ratios

Class F fly ash was used in this study as an aluminosilicate source material and was obtained from Boral, Colorado. Class F fly ash is produced from the combustion of pulverized bituminous or Texas lignite coal and has a low calcium content. The specific gravity of the fly ash is 2.37, and its chemical composition is shown in Table 1. The morphology of the fly ash particles in their original state is shown in Fig. 1. This figure shows that fly ash particles are generally spherical in shape and the diameter of fly ash particles used in this study is in a range of about 500 nm to 30 μm.

The alkaline activator solutions that were used to activate the solid precursor (i.e., fly ash) were prepared by mixing 12 Mole NaOH (sodium hydroxide, SH) solution with Na_2SiO_3 (sodium silicate, SS) solution. SH solution was prepared by dissolving SH pellets with a purity of 98% in distilled water with pH of 7. The SS solution (i.e., silica oxide (SiO_2) of 28% and sodium oxide (Na_2O) of 9% corresponding to a weight ratio of $SiO_2/Na_2O = 3.1$) was chosen for this study. The activator solution was allowed to equilibrate for a minimum of 24 h at a room temperature (23 ± 2 °C) prior to use.

Table 1
The chemical composition of Class F fly ash (% mass).

SiO_2	Al_2O_3	Fe_2O_3	CaO	MgO	SO_3	Na_2O	K_2O	L.O.I[a]
51.82	23.07	13.02	2.79	0.85	1.23	2.29	2.52	2.41

[a] L.O.I. loss on ignition.

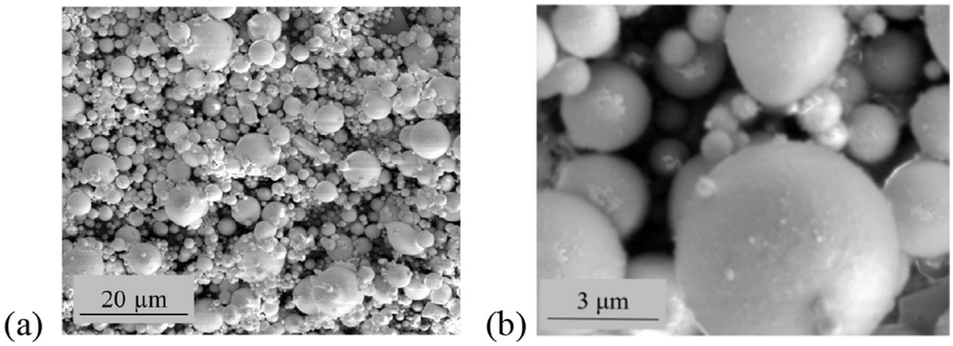

Fig. 1. SEM images of fly ash: (a) particles (2,000×); (b) zoomed view (13,000×).

The ratio of alkaline solution to fly ash was kept constant at 0.4 in order to evaluate the effects of different ratios of alkaline activator on the properties of the interphase region. The Na_2O/SiO_2 ratios attempted were 1.6 and 0.8 for the first mixture (denoted as GP1 hereafter) and the second mixture (denoted as GP2 hereafter), respectively. The ratios of SS to SH for GP1 and GP2 were 1.0 and 2.5, respectively. These ratios were adopted from the experience of previous literature which have reported values such as 0.67–1.0, 1.0, and 2.5, as the optimum SS to SH ratio to produce high strength geopolymer [12,13,42]. The geopolymer concrete specimens were prepared with two different chemical compositions of the alkaline solution. The mix proportion of each and the size distribution of aggregates are shown in Tables 2 and 3, respectively. The fly ash and local crushed limestone were dry-mixed for three minutes, and then the alkaline solution was added and mixed for another five minutes. Since heat is a critical factor to overcome the activation barrier of class F fly ash [43], all specimens were cured at 60 °C for 24 h in a laboratory oven under sealed condition. Then, the specimens were demolded and stored in a controlled environment with temperature of 23 ± 2 °C and relative humidity of 60% for 28 days. The average compressive strength of three samples for GP1 and GP2 was 35.9 MPa and 27.3 MPa, respectively.

2.2. Specimen preparation

2.2.1. Specimen preparation for SEM-EDS and nanoindentation tests

In order to get the best compositional information using SEM-EDS and accurate results from nanoindentation experimentation, it is critical to achieve a sufficiently smooth surface to a tolerable level [44]. Therefore, once each mixture was fully cured, 20 mm thick slices were first cut from concrete samples, and then each piece was cut into small slices of approximately 10 mm × 10 mm cross-section and 4-mm thickness using an MTI digital low-speed diamond saw.

In order to protect the microstructure of the geopolymer material from the stresses induced by mechanical polishing (which is necessary to achieve a highly flat surface), specimens were vacuum impregnated with a low viscosity epoxy resin. When the epoxy hardens, it fills the pores and cracks while maintaining the existing microstructure [45]. After epoxy impregnation, the specimens were ground using a series of silicon carbide-coated papers (340, 400, 600, 800, and 1200 grit) in an automatic grinder-polisher. The grinding time for each grit size was 3 min. After the grinding process, the specimens were cleaned in an ultrasonic cleaner. In the following steps, to make sure the highest surface of the specimen was removed first, diamond lapping films with gradations of 3 μm and 1 μm were used. In order to remove the scratches resulting from previous steps, a sequence of successively finer alumina suspension particles (1 μm, 0.3 μm, and 0.05 μm) was used to polish the surface. Each polishing step lasted approximately 30 min. Finally, an ultrasonic cleaner was used for 5 min to remove all dust and particles remaining from the polishing process.

Table 2
Mix proportions (in kg/m^3) of GP1 and GP2.

Mix	Aggregate	Fly ash	SS	SH
GP1	1,316	774.2	154.9	154.9
GP2	1,316	774.2	221.3	88.5

Table 3
Aggregate gradation in weight percentages.

Particle size (mm)	$4.75 \leq d < 9.5$	$9.5 \leq d < 12.5$	$12.5 \leq d < 19$
Weight %	27	33	40

2.2.2. Specimen preparation for MIP test

The testing specimens of approximately 1.0 cm^3 were cut from the middle of a 100 mm × 200 mm cylinder mixture using a diamond saw. After being cut, the specimens were immersed in ethanol for 24 h to cease any further chemical reactions. Then the specimens were dried in an oven at 70 °C for 4 h.

2.2.3. Specimen preparation for three-point bending test

Due to its simplicity, the three-point bending SENB specimen was chosen to investigate the effect of interphase on fracture-related indicators from testing results. The SENB is an attractive test as specimens are easy to fabricate without complicated tools, and testing can be conducted on a typical three-point bending mode. The testing configuration of the SENB is shown in Fig. 2 and comprised of notched beam specimens with 120 mm wide, 40 mm thick and 60 mm height. Each testing specimen had 2 mm wide pre-crack (notch) in middle. Two types of testing specimens were prepared for paste-only (Fig. 2(a)) and paste-aggregate interface (Fig. 2(b)) fracture. The single aggregate used for paste-aggregate interface specimens was cut by diamond saw from core samples of limestone. The aggregate in the middle of specimens had 55 mm height, 40 mm wide and 5 mm thick. The middle of the specimen is considered an adhesive interfacial zone which is prone to fracture during testing.

3. Testing and analysis methods

3.1. SEM-EDS test

The polished surface of the specimens was imaged under FEI Nova NanoSEM coupled with EDS to acquire micrographs that distinguish different solid phases and to characterize chemical compositions of each phase. After 28 days of curing, several high-resolution images were obtained from each specimen. Image analysis was performed using MIPAR software in order to quantify the area fractions of distinct phases in two different regions: region 1 which is considered more likely an interphase by taking 50 μm strips parallel to the aggregate faces, and region 2 which is considered a paste by taking the region from the 50 μm strips. To separate the phases within the image, a grey-level threshold value was set and used; however, it was not accurately accomplished because multiple different phases present in the image were in a similar grey level. Manual adding or removing of the areas that were needed or unwanted were thus applied to resolve the issue, and the SEM images were converted into binary images to distinguish into two primary phases: N-A-S-H (in a continuous phase) in black and the other phases (in a distinctive phase) in white. By using the measurement tool, the area percentages of individual phases were quantified.

3.2. Nanoindentation test

The elastic moduli of 28-day cured GP specimens were characterized with a grid nanoindentation technique. Three representative areas of similar sizes were selected randomly around the aggregates. In each area, 240 indentations were carried out in a grid of 140 μm × 150 μm with 10 μm distance between indents. The grid of a representative testing area is shown in Fig. 3. The testing area was divided into two regions: a region with a dimension of

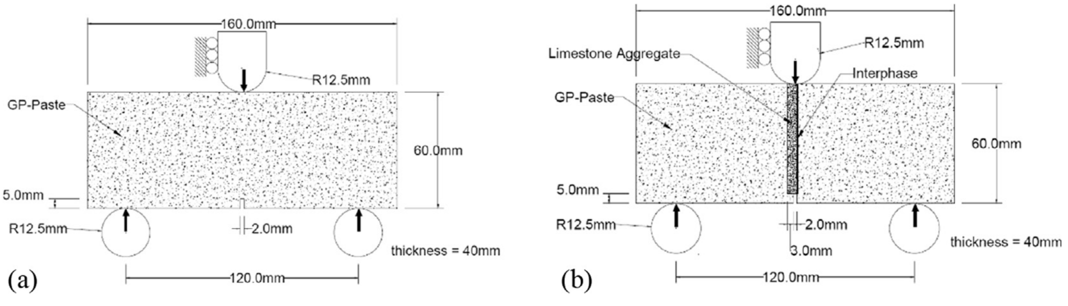

Fig. 2. Experimental configuration for SENB test: (a) for specimens of paste-only (b) for specimens with aggregate inserted in the middle.

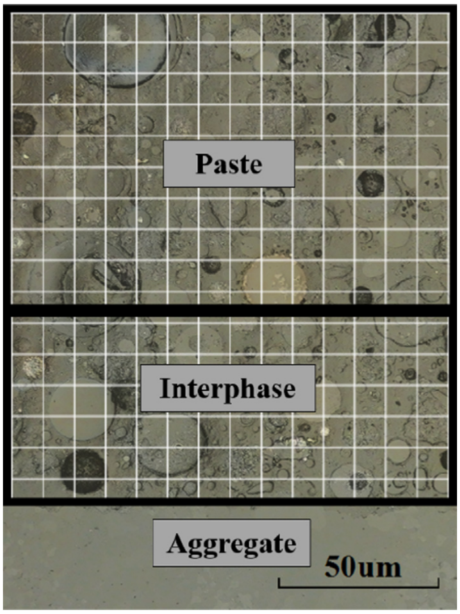

Fig. 3. The representative area of the nanoindentation test.

$140\ \mu m \times 50\ \mu m$ around the aggregate, which is representative of the interphase region between aggregate and paste, and a region with a dimension of $140\ \mu m \times 100\ \mu m$, which is representative of paste. The dimension of region 1 set to be 50 μm is consistent with the SEM image analysis, and it is typically regarded as a size of ITZ in OPC [46].

The nanoindentation tests were performed by a Hysitron Triboindentor with a pyramidal-shaped diamond Berkovich tip. As is the case with most instruments, calibration is of great significance because it limits uncertainties and yields repetitive results. Tip-shape calibration is primarily based on the determination of an area function for the selected probe. This method assumes that the sample modulus is independent of indentation depth. Fused silica was used as the standard material for calibration in this study. The loading function was a quasi-static load-controlled mode which was performed in 10-s up to a maximum load of 2,000 μN at a rate of 200 μN/s, followed by a 5-s hold and 10-s unloading at the same rate. The 5-s holding period was considered to eliminate any potential creep effects.

For characterizing nanomechanical properties, the Oliver and Pharr method [47] was used by fitting the load–displacement curve as shown in Fig. 4. The reduced modulus (E_r) that captures the effect of both the elastic deformation of the selected test specimen and the indenter [48] is defined as follows:

$$E_r = \frac{1}{\beta} \cdot \frac{S}{2} \cdot \frac{\sqrt{\pi}}{\sqrt{A_c}} \tag{1}$$

where the parameter S refers to the contact stiffness of the material and is defined as the initial slope of the unloading part of the load vs. indentation curve at $h = h_{max}$. The A_c is the projected area at the peak load (P_{max}), and β is a dimensionless correction factor that accounts for the shape of the indenter tip and is assumed as 1.081 for the Berkovich indenter tip used in this study.

The elastic deformation effect of the indenter is assumed to be known so that the absolute elastic modulus (E_s), which is solely responsible for the indentation depth recovery during the unloading process, can be determined. This relation is given by:

$$\frac{1}{E_r} = \frac{1 - \nu_s^2}{E_s} + \frac{1 - \nu_i^2}{E_i} \tag{2}$$

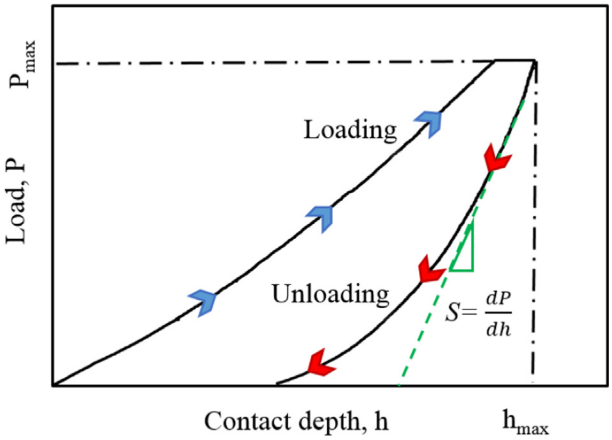

Fig. 4. Schematic of load–displacement curve from nanoindentation.

where E and ν are Young's modulus and Poisson's ratio, respectively; here the subscripts correspond to the specimen (s) and diamond indenter tip (i). The elastic modulus and Poisson's ratio of the diamond indenter are equal to 1,140 GPa and 0.07, respectively. The Poisson's ratio of geopolymer was assumed to be 0.2 [20].

3.3. Statistical deconvolution of nanoindentation results

To determine individual properties of heterogeneous materials, a statistical deconvolution technique can be applied to a histogram of properties measured [20,49]. The histogram of E is constructed from the effective measurements with the number of N_{exp} that are divided into N_{bins} with an equal spacing of size b. The experimental probability density function (PDF) can then be computed as shown in Eq. (3).

$$p_i^{exp} = \frac{f_i^{exp}}{N_{exp}} \cdot \frac{1}{b};\ i = 1\ ,2,\ \ldots,\ N_{bins} \tag{3}$$

where p_i^{exp} is the experimental PDF of bin i and f_i^{exp} is the frequency of the property (such as E in this case) within bin i in all effective indentation measurements. In this study, the bin size was set at 1.5 GPa for the elastic modulus. By applying the deconvolution method, individual PDFs related to individual phases can be found.

The elastic modulus of each phase was assumed to follow a normal distribution:

$$p_r(x) = \frac{1}{\sqrt{2\pi s_r^2}} \exp \frac{-(x - \mu_r)^2}{2s_r^2} \tag{4}$$

where r is the mechanical properties related to single material phases, p_r is the theoretical PDF of the rth phase, and μ_r and s_r are the mean value and standard deviation of the rth phase computed from N_r values as follows:

$$\mu_r = \frac{1}{N_r} \sum_{k=1}^{N_r} x_k, \tag{5}$$

$$s_r^2 = \frac{1}{N_r - 1} \sum_{k=1}^{N_r} (x_k - \mu_r)^2;\ k = 1, \ldots, N_r \tag{6}$$

where x is the approximated E value related to the rth phase.

The theoretical PDF covering all M phases (as illustrated in Fig. 5) is then:

$$C(x) = \sum_{r=1}^{M} f_r p_r(x), \tag{7}$$

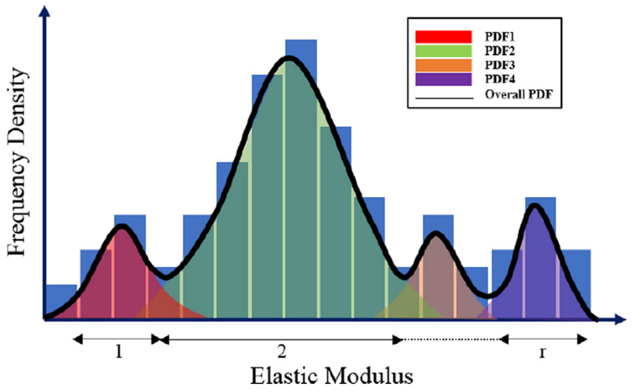

Fig. 5. Construction of *M* probability density functions from the experimental data.

where f_r is the volume fraction of the *rth* phase and is equal to N_r/N_{exp}. It should be noted that entire volume fraction of all *M* phases is equal to 1.0.

The theoretical PDF of each phase is then determined by minimizing the following error function:

$$\min\sum_{i=1}^{N^{bins}}\left[\left(P_i^{\mathrm{exp}}-C(x_i)\right)P_i^{\mathrm{exp}}\right]^2 \tag{8}$$

3.4. Mercury intrusion porosimetry (MIP) test

The porosity and pore size distribution of 28-day cured geopolymer pastes were measured by mercury intrusion porosimetry (MIP) using a Quantachrome PoreMaster 60 with a maximum intruding pressure of 420 MPa corresponding to a minimum pore size of 3 nm. An autorun mode was chosen with surface tension and a contact angle of 0.48 N/m and 140°, respectively. The principle of the MIP is to progressively record the intrusion mercury volume at each pressure point until it reaches the maximum pressure. At the maximum pressure, the total porosity can be obtained by dividing the total intruded mercury volume by the volume of the sample. The applied pressure at each point can be related to the corresponding pore diameter; then the pore diameter can be calculated by using Washburn equation [50].

3.5. Three-point bending test

The three-point bending test was conducted using an ElectroForce dynamic mechanical station fitted with a load cell of 3 kN capacity. As Fig. 2 illustrates, each SENB specimen was manufactured by casting GP mixtures into an in-house mold to target specimen geometry also shown in Fig. 2. After curing for 28 days, each hardened GP specimen was placed on the three-point bending fixture. After trial and error, it was found that applying a small contact load (i.e., 2 N) ensured good contact between the testing specimen and the crosshead (loading point). Subsequently, each beam specimen was loaded at 0.001 mm/s loading rate until complete failure. A total of five to six specimens were tested for each case.

4. Results and discussion

4.1. Microstructural and chemical characteristics

The representative microstructure of the geopolymer mixtures with different mixing ratios are presented in Fig. 6. These SEM

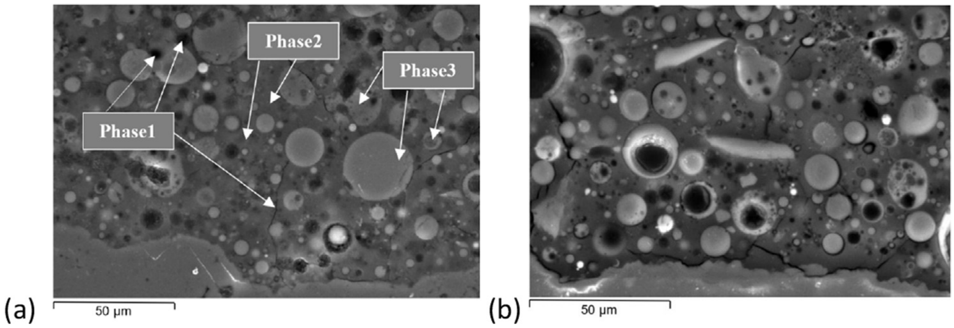

Fig. 6. SEM images of geopolymer activated with different Na_2O/SiO_2: (a) GP1; (b) GP2.

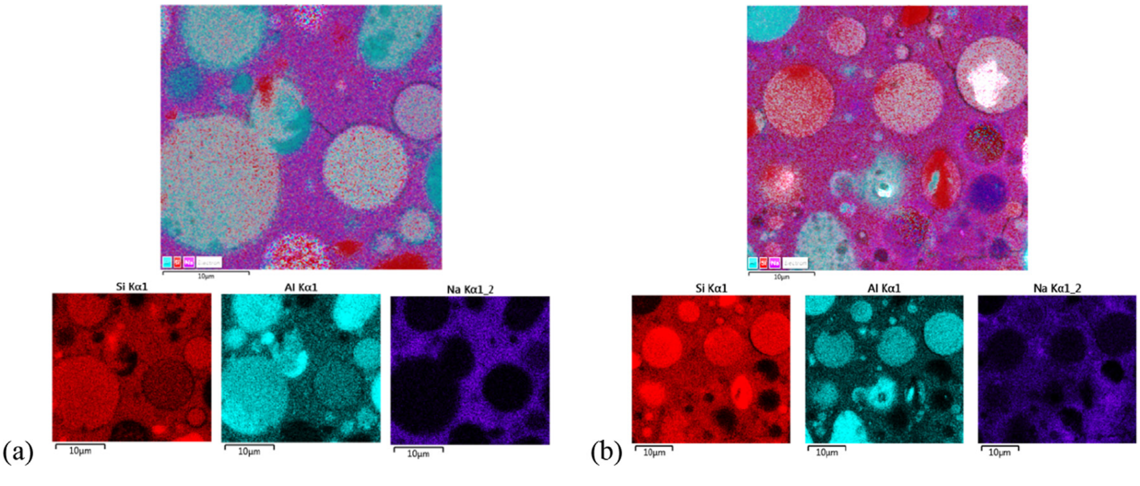

Fig. 7. EDS map analysis of: (a) GP1; (b) GP2.

images display the presence of multiple phases. The presence of N-A-S-H gel and fly ash particles was confirmed by EDS analysis as it is shown in Fig. 7. This figure shows the EDS overlay map and the individual maps of Si, Al, and Na. Since geopolymer is mainly (around 85%) composed of Si, Al, and Na, the maps of only these three elements are presented for the sake of simplicity. The higher concentration of each color shows the higher concentration of each element in the map.

The first phase (denoted as Phase 1 hereafter) which is associated with the vacancy (cracks and voids) appears black in the SEM image because of its low mean atomic number. It should be noted that some of the pores are formed within some fly ash particles which were originally hallow (cenospheres) [51]. The second phase (denoted as Phase 2 hereafter), which is distributed uniformly in dark grey in the microstructure, is attributed to the sodium aluminosilicate hydrate (N-A-S-H) gel. This was confirmed by EDS analysis, which shows the continuous layer appeared in purple in the Na map. The N-A-S-H gel is the most important reaction product in geopolymer material and acts as a binding agent that embeds all of the remaining phases. This gel has been characterized extensively by many studies including [40,52,53]. There are other phases of fly ash particles in different levels of reaction (such as unreacted fly ash particles, fly ash particles with cavities, and partially reacted particles [54]) appear light grey in the microstructure and are considered as Phase 3 in this study. The fly ash particles presented bright in Si and Al maps due to the high concentration of these two elements and dark in the Na map.

The area fractions of individual phases (Phase 1, Phase 2, and Phase 3) resulting from six images of GP1 and eight images of GP2 in the two regions (i.e., region 1 and region 2) are shown in Table 4. As shown, the area fractions of Phase 2 at the region 1 (close to aggregate surface) are 70.5% and 63.1% for GP1 and GP2, respectively. The area fractions of Phase 2 at the region 2 (farther from the aggregate surface) are 58.5% and 49.3% for GP1 and GP2, respectively. The results infer that the area percentages of different phases are influenced by the Na_2O/SiO_2 ratio. This might be due to the fact that the alkaline solution with a higher sodium content leads to the dissolution of more fly ash particles, then transforms them into N-A-S-H gel (binding phase). The test results of image analysis also demonstrate that the geopolymer matrix contains richer N-A-S-H gel in the proximity (region 1) of aggregate particles than in the paste region (region 2), which is the different observation of the case of conventional OPC mixture where less C-S-H gel is typically formed at the interphase [3].

Table 5 shows EDS results on the points shown in Fig. 8(a) and (b). The EDS point analysis was performed to investigate the composition of some unreacted fly ash particles and N-A-S-H gel in GP1 and GP2. Table 5 shows that the Si/Al ratios of the N-A-S-H gel (points 1, 2, 3 in Fig. 8) is higher than that of fly ash particles (points 4, 5, 6 in Fig. 8) in both cases. The Si/Al ratios of the N-A-S-H gel is higher than that of fly ash particles since the Si in N-A-S-H gel comes from both the alkaline activator and the dissolved fly ash particles, while Al only comes from the fly ash particles. The Na/Al in N-A-S-H gel is also much higher than that of unreacted fly ash particles since Na is provided by the alkaline activator during geopolymeric reaction. As expected, the Na content in GP1 was higher than the Na content in GP2 due to higher Na_2O/SiO_2 ratio in GP1.

4.2. Nanomechanical properties

Overall nanoindentation results from each region (i.e., interphase and paste) for GP1 and GP2 specimens were merged and plotted in Fig. 9. It shows the overall experimental (with actual data) and theoretical (with smoothing) probability density functions (PDFs) with deconvoluted five peaks in GP1 and GP2 specimens on both regions. The histogram covers all the phases present in geopolymer material. Based on the understanding from previous studies that identified distinct phases created in fly-ash based geopolymers [51,55], the deconvoluted peaks were assigned to the individual phases. The first peak with the lowest elastic modulus can be attributed to the phase with a lack of materials such as voids and cracks, whereas the last peak (Peak 5) with the highest elastic modulus is highly related to the phase with unreacted fly ash particles. The second peak, which is the largest and most frequent, is most likely associated with N-A-S-H gel, which is the main binding phase in geopolymer. The third peak is attributed to the partially reacted fly ash particles with the reaction products remaining around the particles, hence a higher elastic modulus than N-A-S-H gel, which has diffused away from the fly

Table 4
Area fraction (%) of different phases in the two regions.

Specimen	Region	Phase 1	Phase 2	Phase 3
GP1	Region 1	1.5 + 0.79	70.5 + 5.83	28.1 + 5.35
	Region 2	1.4 + 0.38	58.5 + 4.88	40.1 + 5.11
GP2	Region 1	2.5 + 0.85	63.1 + 11.25	34.4 + 11.64
	Region 2	2.6 + 1.00	49.3 + 5.58	48.1 + 6.06

Table 5
EDS point analysis results of GP1 and GP2.

Sample	Point	Si (%)	Al (%)	Na (%)	Si/Al	Na/Al
GP1	1	57.0	22.3	20.7	2.56	0.93
	2	58.3	21.1	20.6	2.76	0.98
	3	57.6	21.8	20.6	2.64	0.94
	4	63.1	36.1	0.8	1.75	0.02
	5	68.1	29.2	2.7	2.33	0.09
	6	56.0	43.2	0.8	1.30	0.02
GP2	1	67.8	19.8	12.4	3.42	0.63
	2	66.7	19.9	13.4	3.35	0.67
	3	69.9	18.4	11.7	3.80	0.64
	4	53.3	42.4	4.3	1.26	0.10
	5	53.2	42.1	4.7	1.26	0.11
	6	67.7	29.3	3.0	2.31	0.10

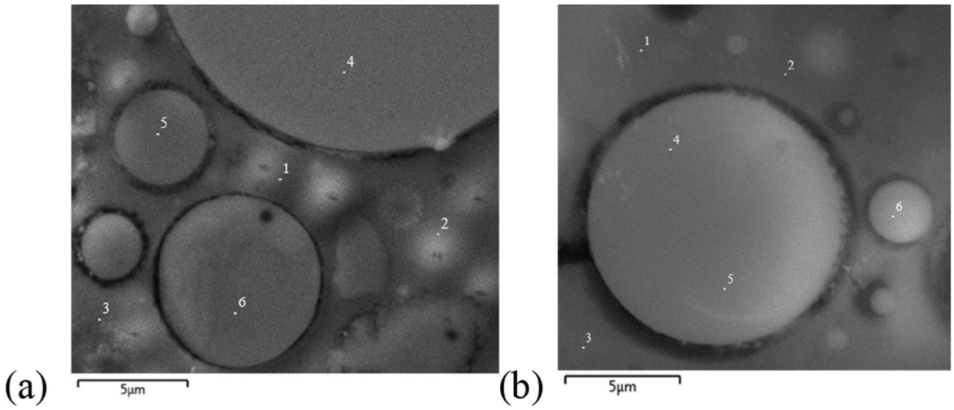

Fig. 8. SEM images showing EDS points of analysis on: (a) GP1; (b) GP2.

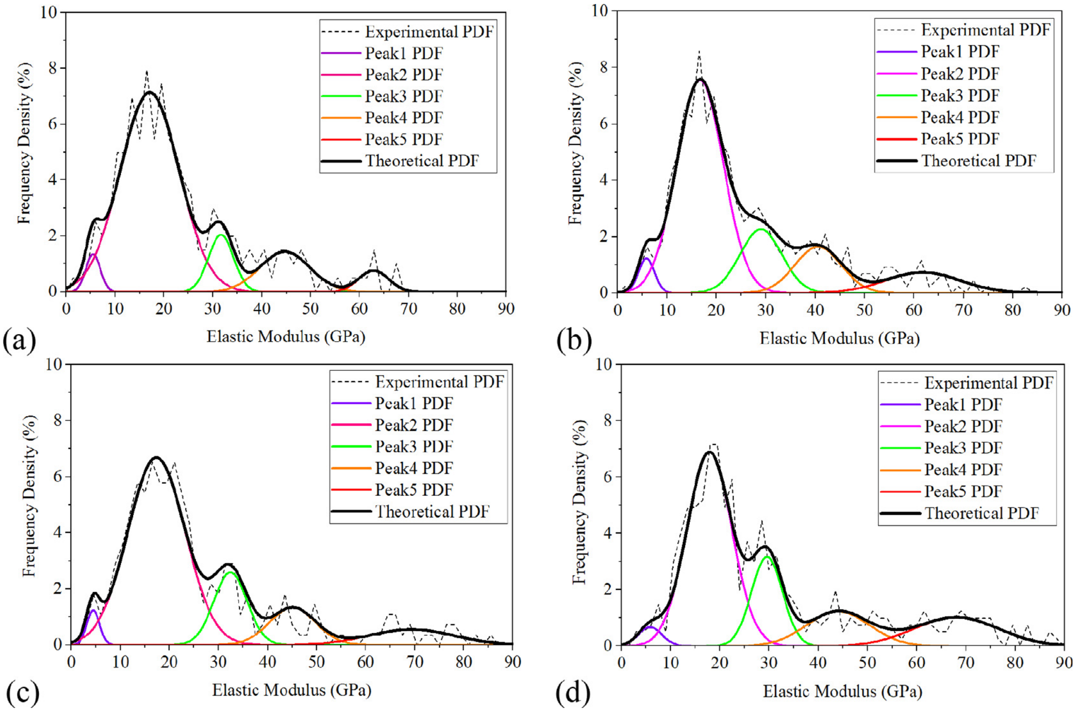

Fig. 9. Deconvolution results of the PDF of elastic modulus for the GP1: (a) region 1 (interphase), (b) region 2 (paste); and GP2 (c) region 1 (interphase), (d) region 2 (paste).

ash particles is exhibited. The fourth peak, although it is not conclusive at this stage, based on matching with SEM image analysis results, it seems related to unreacted fly ash particles containing some cavities that lead to lower stiffness than the intact fly ash particles. Some relevant previous studies have reported similar values of elastic moduli [20,51].

The mean elastic moduli of individual peaks and their frequency of occurrence resulting from GP1 and GP2 are summarized in Table 6. As can be inferred from the table, the elastic modulus of N-A-S-H gel is around 16–17 GPa regardless of the Na_2O/SiO_2 of the activator, while the frequency of occurrence of the produced gel is apparently dependent on the Na_2O/SiO_2. The GP1 specimen with a higher Na_2O content in the activator produced more N-A-S-H gel than GP2 specimen. The percentage of N-A-S-H gel in the region 1 (interphase) and region 2 (paste) of the GP1 specimen was around 12% higher than that of GP2 specimen. Comparing the frequency of occurrence of N-A-S-H gel in the two regions, it was observed that the N-A-S-H gel in region 1 was more than that of region 2 in both GP1 and GP2. This observation agrees well the results of SEM image analysis.

The quantified fraction of the first peak (the phase with a lack of materials such as voids and cracks) in the GP1 was slightly higher than that of GP2; however, nanoindentation may not be a proper way to determine the volumetric fraction of such phase in the specimens. Therefore, the pore structure of each specimen was evaluated by the MIP, which is a common method used to investigate internal pores of conventional cementitious materials [56–58].

4.3. Pore structure analysis

The effects of different alkaline solution compositions on the pore structure of geopolymer were studied by measuring the distribution of pore sizes and porosity using MIP. Fig. 10(a) shows the curves of cumulative intrusion volume and pore diameters of GP1 and GP2. As presented, the cumulative intruded mercury

Table 6
Elastic moduli of individual phases and their frequency of occurrence.

		Peak 1	Peak 2	Peak 3	Peak 4	Peak 5
GP1-region 2	*E* (GPa)	5.83 ± 1.82	16.66 ± 5.64	29 ± 4.52	40.55 ± 4.62	61.73 ± 7.29
	Freq (%)	3.28	59.04	15.77	12.69	9.20
GP1-region 1	*E* (GPa)	5.50 ± 1.58	17.07 ± 5.86	31.65 ± 3.04	44.71 ± 5.21	62.86 ± 3.10
	Freq (%)	3.33	71.95	8.67	12.21	3.82
GP2-region 2	*E* (GPa)	5.82 ± 1.87	17.87 ± 5.97	29.57 ± 3.69	44.01 ± 7.15	68.06 ± 9.17
	Freq (%)	2.67	52.83	16.83	13.13	14.53
GP2-region 1	*E* (GPa)	4.44 ± 1.66	17.34 ± 5.73	32.42 ± 3.84	45.06 ± 5.31	69.32 ± 8.01
	Freq (%)	2.64	64.68	14.56	10.32	7.78

volume of GP1 was not significantly lower than that of GP2, and the pore size distributions did not change much by varying the ratio of Na_2O/SiO_2. The total porosity could be calculated from the cumulative intruded mercury volume. The resulting total porosity was 29.65% and 34% for GP1 and GP2, respectively. It can be implied from the results that increasing the sodium content might lead to the reduced porosity of geopolymer materials. 65% of measured pores in GP1 was within a range of 0.0036–0.05 μm, whereas only 40% of measured pores in GP2 was within that range. In addition, the volumetric percentages of pores within a range of 0.05–0.2 μm were 23% and 51% for GP1 and GP2, respectively. The results of MIP are in line with the results from the SEM image analysis where GP1 had more N-A-S-H and fewer pores than GP2. With a high content of sodium in the alkaline solution such as in GP1, the more N-A-S-H gel could be produced, which would lead to more refinement of pore structure.

Fig. 10(b) shows the differential pore distribution curves of GP1 and GP2. Two primary peaks were observed, which is similar to the differential curves observed from traditional cement paste [59]. The two primary peaks reflect the presence of two pore systems: the capillary pores and gel pores, and the first peak identifies the critical pore diameter. The critical pore diameter has been reported to largely influence the permeability and diffusion of traditional cementitious materials [60,61]. It was found that the critical pore diameter was 42 nm and 62 nm for GP1 and GP2, respectively. Increasing the ratio of Na_2O/SiO_2 in the alkaline solution led to a reduction in the critical pore size.

4.4. Three-point bending test results

Since the roughness of the aggregate plays an important role in the aggregate-paste interaction [62–64], the roughness of the aggregates used for GP1 and GP2 was determined in multiple locations using a laser scanning microscope before conducting three-point bending fracture test [65]. The 3D topographic images of the scanned area of the aggregate used for making GP1 and GP2 specimens are shown in Fig. 11. The average root mean square (RMS) values of 15 scans for each representative aggregate are shown in Table 7. A statistical *z*-test was performed to compare the roughness of the aggregates, and it was found out that the average roughness of the aggregates for GP1 and GP2 were not significantly different (i.e., $P > 0.05$).

As aforementioned, the three-point bending test was conducted in displacement-controlled mode using an Electroforce dynamic mechanical station which permitted loading to be applied at a slow rate (0.001 mm/s) to achieve the quasi-static condition. Data were recorded at a fast rate (20 data points per second) to ensure accuracy. Fig. 12 presents load point displacements plotted against the applied forces from all the cases (i.e., GP1 and GP2, both with and without aggregate). It can be noted that the mechanical behavior of GP SENB specimens was generally elastic and failed in a brittle fashion. Results show that in all cases, the maximum load was more repeatable compared to the displacement at which the specimens failed.

For a more quantitative assessment, data analysis was conducted from the test results presented in Fig. 12 by identifying four indicators: the maximum load, displacement at failure, stiffness, and the interfacial bond strength (IBS). The IBS was calculated only for the GP specimens with aggregate by dividing the maximum load by the cross-sectional area of the aggregate (i.e., $55 \times 40\ mm^2$). Analysis results are shown in Table 8 with the average values and standard errors. As shown in the table, the maximum load and displacement at failure of beams with only paste were greater than beams with the aggregate inserted. This indicates that the interfacial bonding between the paste and aggregate influences the mechanical properties of concrete. Table 8 also shows that increasing the molar ratio of Na_2O/SiO_2 in the alkaline solution clearly affected the IBS between paste and aggregate. The IBS of GP1 was much greater than that of GP2. This might be due to more N-A-S-H gel produced in the proximity of aggregate particles in GP1 than GP2, which was observed from the SEM-EDS microstructural image and nanoindentation test-analysis results in this study. Regarding mixture stiffness, GP2 presented higher values than GP1 when the beam is paste-only. This observation was somewhat different from the initial expectation, since more N-A-S-H gel formation was observed from GP1 than GP2. It is not

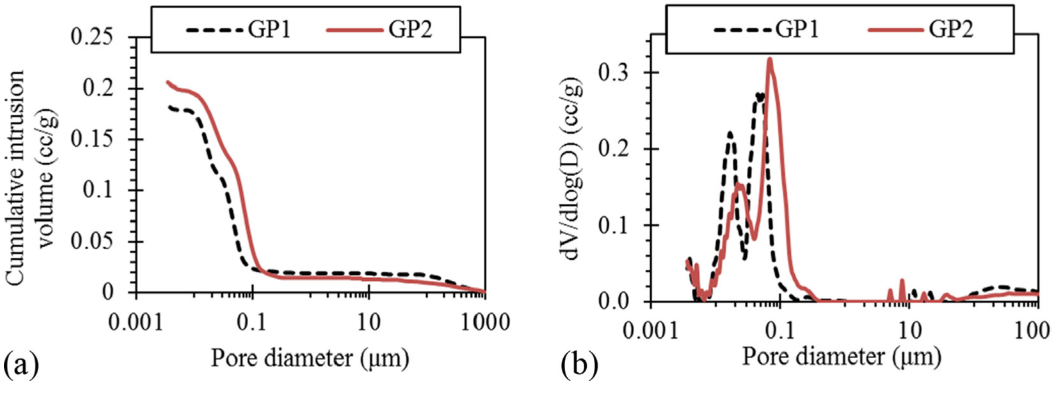

Fig. 10. Pore size distribution: (a) cumulative curve; (b) differential curve.

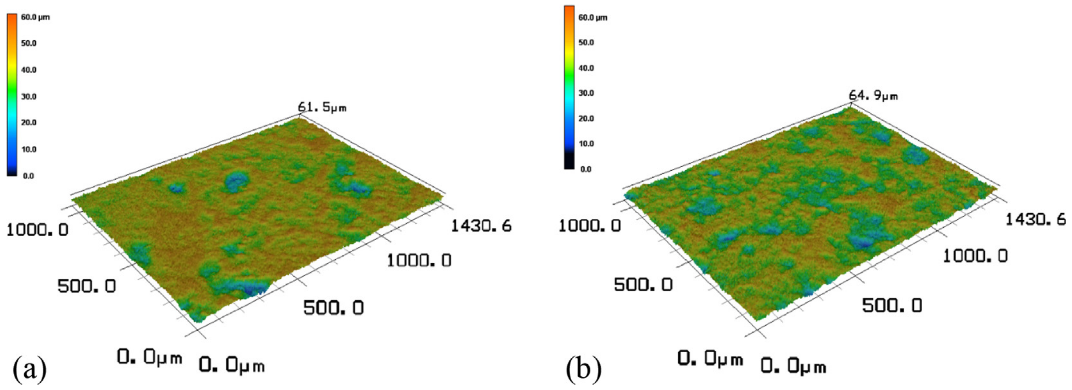

Fig. 11. The 3D topographic image of the aggregate used for: (a) GP1; (b) GP2.

Table 7
RMS roughness measurements (µm).

Samples	Scanning size	Average RMS roughness	RMS roughness deviation
GP1	1,430*1,000	7.11	0.85
GP2	1,430*1,000	6.95	0.83

certain why GP2 paste was stronger than GP1 paste at this stage, but the definite conclusion should be made with more statistically ample test results. As shown in Fig. 12, test results between replicates showed a variability, which certainly limits the conclusive assessment.

Although more data and further analyses are necessary to reach more definite conclusions, the results summarized in Table 8

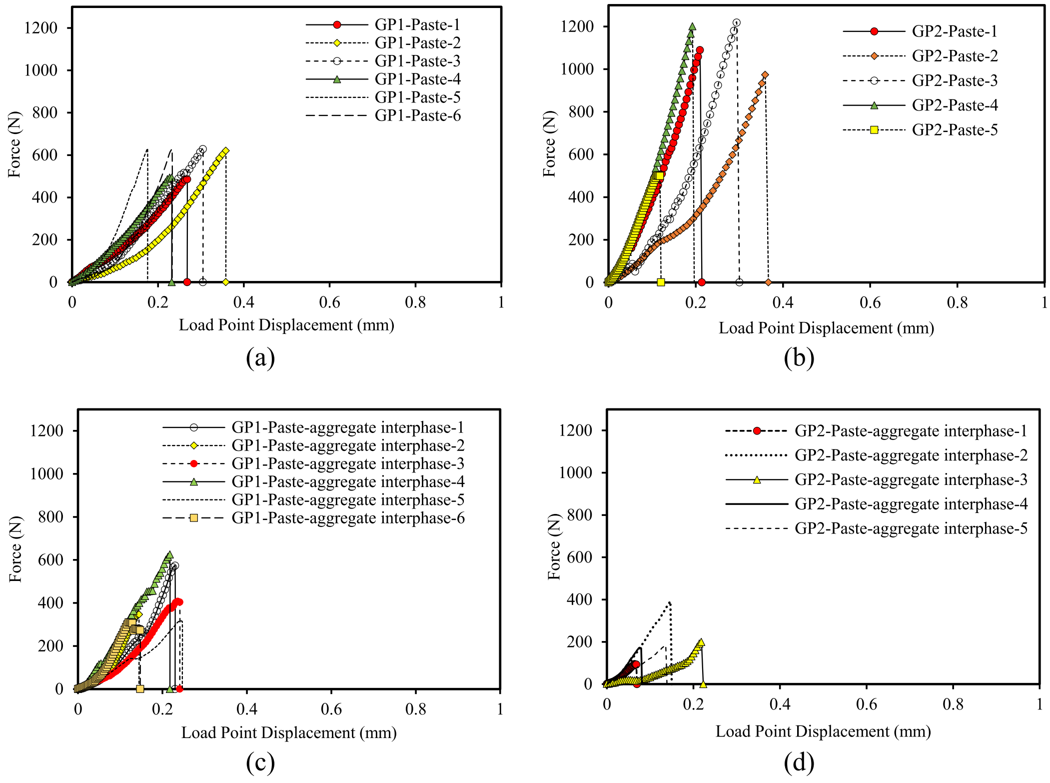

Fig. 12. Three-point bending test results of SENB: (a) GP1: paste-only; (b) GP2: paste-only; (c) GP1: paste-aggregate; and (d) GP2: paste-aggregate.

Table 8
Analysis results from the SENB test for all cases tested with associated standard error.

Mix	Case	Maximum load (N)	Displacement at failure (mm)	Stiffness (N/mm)	IBS (MPa)
GP1	Paste-only	582.65 ± 11.68	0.26 ± 0.01	2,441.43 ± 144.13	Not applicable
	Interphase	432.51 ± 23.19	0.2 ± 0.007	2,458.76 ± 155.03	0.19 ± 0.01
GP2	Paste-only	1,012.25 ± 59.83	0.23 ± 0.01	4,570.53 ± 340.7	Not applicable
	Interphase	209.79 ± 22.19	0.13 ± 0.01	1,909.77 ± 188.7	0.09 ± 0.01

implies that the higher content of unreacted fly-ash particles in GP2 stiffens the paste of the mixture but produces a weaker interphase. Conversely, when a mixture allows increased reaction to occur such as in GP1, the resulting paste is less stiff but beneficial to the strength of the paste-aggregate interphase since the reaction product (i.e., N-A-S-H gel) acts as a binding agent that bonds aggregate and paste tightly together.

5. Concluding remarks

This study investigated the effects of different Na_2O/SiO_2 molar ratios on the mechanical and microstructural characteristics of the aggregate-paste interphase in fly ash-based geopolymer concrete mixtures. The following conclusions can be drawn based on test-analysis results.

- The analysis of the SEM images identified three major phases in the microstructure of the geopolymer mixture at varied fractions: phase with a lack of materials (e.g., voids and cracks), N-A-S-H gel phase, and fly ash particles with different levels of reaction. The N-A-S-H gel occupied the largest area fraction among others and was observed more in the proximity of aggregate particles than in the paste. Higher molar ratios of Na_2O/SiO_2 in the alkaline solution led to the formation of more N-A-S-H gel and fewer pores. A detailed comparison of pore structure features using the MIP also showed that the critical pore size decreases by increasing the molar ratio of Na_2O/SiO_2 in the alkaline solution.
- From the nanoindentation testing, five distinct peaks in the distribution of elastic moduli were usually identified through the deconvolution technique. The first and second peaks were attributed to the pores and N-A-S-H gel, respectively. Other three peaks were related to fly ash particles in different levels of curing-reaction with the alkaline solution. The elastic modulus of the main reaction product (N-A-S-H gel) was in a range of 16–17 GPa and seemed to be independent of the alkaline solution molar ratio. The nanoindentation results also confirmed the existence of a rich generation of N-A-S-H gel in the proximity of aggregate particles compared to the paste, regardless of the Na_2O/SiO_2 molar ratios attempted in this study.
- From the results of three-point bending of SENB specimens, it was observed that the mechanical performance of the geopolymer mixtures mainly depends on the fraction of N-A-S-H gel. The interfacial behavior of GP1 was better than GP2, which seems due to more N-A-S-H gel produced in the proximity of aggregate particles in GP1 than GP2. In general, large-scale mechanical test results were in a good agreement with other small-scale results. The higher amount of Na_2O/SiO_2 molar ratio exhibited more N-A-S-H gel in the interphase, which led to increased bonding between aggregate and geopolymer paste.
- For a more conclusive understanding, more testing variables including different Na_2O/SiO_2 molar ratios than the two ratios attempted in this study should be considered. In addition, more test results that can allow rigorous statistical assessments should be pursued. Further efforts to cohesively incorporate multiscale results and observations (i.e., SEM, nanoindentation, pore structure, EDS, and three-point bending) from the geopolymer materials and control ordinary Portland cement materials are also significant, which is in progress by the authors.

6. Compliance with ethical standards

6.1. Ethical responsibilities of authors

This manuscript represents original work that is not being considered for publication, in whole, in another journal, book, conference proceedings, or government publication. All previously published work cited in the manuscript has been fully acknowledged. This manuscript is one of a kind, or part of a study or thesis from which other manuscripts may be generated. All of the authors have contributed substantially to the manuscript and approved the final submission.

6.2. Consent informed

This research did not involve any human participants and/or animals.

Conflict of interest

The authors declare that they have no conflict of interest.

Acknowledgements

The authors are grateful for the financial support received from the National Science Foundation (Grant No. CMMI-1635055). We also like to acknowledge testing facilities: The Nano-Engineering Research Core Facility (NERCF) and the Nebraska Center of Materials and Nanoscience (NCMN) at the University of Nebraska-Lincoln to conduct the laboratory tests for this study.

References

[1] K.L. Scrivener, A.K. Crumbie, P. Laugesen, The interfacial transition zone (ITZ) between cement paste and aggregate in concrete, Interface Sci. 12 (4) (2004) 411–421.
[2] D.P. Bentz, E.J. Garboczi, E. Schlangen, Computer simulation of interfacial zone microstructure and its effect on the properties of cement-based composites, Am. Ceram. Soc. Mater. Sci. Concr. 6 (1995).
[3] P. Mondal, Nanomechanical Properties of Cementitious Materials, Northwestern University, 2008.
[4] T. Akçaoğlu, M. Tokyay, T. Çelik, Assessing the ITZ microcracking via scanning electron microscope and its effect on the failure behavior of concrete, Cem. Concr. Res. 35 (2) (2005) 358–363.
[5] S. Erdem, A.R. Dawson, N.H. Thom, Influence of the micro-and nanoscale local mechanical properties of the interfacial transition zone on impact behavior of concrete made with different aggregates, Cem. Concr. Res. 42 (2) (2012) 447–458.
[6] D.P. Bentz, Influence of silica fume on diffusivity in cement-based materials: II. Multi-scale modeling of concrete diffusivity, Cem. Concr. Res. 30 (7) (2000) 1121–1129.
[7] P. Simeonov, S. Ahmad, Effect of transition zone on the elastic behavior of cement-based composites, Cem. Concr. Res. 25 (1) (1995) 165–176.
[8] P. Nath, P.K. Sarker, Use of OPC to improve setting and early strength properties of low calcium fly ash geopolymer concrete cured at room temperature, Cem. Concr. Compos. 55 (2015) 205–214.
[9] J. Davidovits, Geopolymer, Green Chemistry and Sustainable Development Solutions: Proceedings of the World Congress Geopolymer 2005, Geopolymer Institute, 2005.
[10] J. Davidovits, Geopolymers: inorganic polymeric new materials, J. Therm. Anal. Calorim. 37 (8) (1991) 1633–1656.
[11] P. Chindaprasirt, P. De Silva, K. Sagoe-Crentsil, S. Hanjitsuwan, Effect of SiO2 and Al2O3 on the setting and hardening of high calcium fly ash-based geopolymer systems, J. Mater. Sci. 47 (12) (2012) 4876–4883.
[12] P. Chindaprasirt, T. Chareerat, V. Sirivivatnanon, Workability and strength of coarse high calcium fly ash geopolymer, Cem. Concr. Compos. 29 (3) (2007) 224–229.
[13] M. Morsy, S. Alsayed, Y. Al-Salloum, T. Almusallam, Effect of sodium silicate to sodium hydroxide ratios on strength and microstructure of fly ash geopolymer binder, Arabian J. Sci. Eng. 39 (6) (2014) 4333–4339.
[14] A. Palomo, M. Grutzeck, M. Blanco, Alkali-activated fly ashes: a cement for the future, Cem. Concr. Res. 29 (8) (1999) 1323–1329.
[15] M. Khedmati, Y.-R. Kim, J.A. Turner, H. Alanazi, C. Nguyen, An integrated microstructural-nanomechanical-chemical approach to examine material-specific characteristics of cementitious interphase regions, Mater. Charact. (2018).
[16] M. Ariffin, M. Bhutta, M. Hussin, M.M. Tahir, N. Aziah, Sulfuric acid resistance of blended ash geopolymer concrete, Constr. Build. Mater. 43 (2013) 80–86.
[17] D.V. Reddy, J.-B. Edouard, K. Sobhan, Durability of fly ash–based geopolymer structural concrete in the marine environment, J. Mater. Civ. Eng. 25 (6) (2012) 781–787.
[18] S.H. Sanni, R. Khadiranaikar, Performance of geopolymer concrete under severe environmental conditions, Int. J. Civ. Struct. Eng. 3 (2) (2012) 396.

[19] A. Fernández-Jiménez, A. Palomo, M. Criado, Microstructure development of alkali-activated fly ash cement: a descriptive model, Cem. Concr. Res. 35 (6) (2005) 1204–1209.

[20] J. Němeček, V. Šmilauer, L. Kopecký, Nanoindentation characteristics of alkali-activated aluminosilicate materials, Cem. Concr. Compos. 33 (2) (2011) 163–170.

[21] G.S. Ryu, Y.B. Lee, K.T. Koh, Y.S. Chung, The mechanical properties of fly ash-based geopolymer concrete with alkaline activators, Constr. Build. Mater. 47 (2013) 409–418.

[22] K.Z. Rami, Y.-R. Kim, M. Khedmati, G. Nsengiyumva, H. Alanazi, Two-way linked multiscale method integrated with nanomechanical tests and cohesive zone fracture to model highly heterogeneous binding materials, J. Eng. Mech. 144 (10) (2018) 04018095.

[23] J. Swanepoel, C. Strydom, Utilisation of fly ash in a geopolymeric material, Appl. Geochem. 17 (8) (2002) 1143–1148.

[24] H. Xu, J. Van Deventer, The geopolymerisation of alumino-silicate minerals, Int. J. Miner. Process. 59 (3) (2000) 247–266.

[25] H. Xu, J.S. Van Deventer, Geopolymerisation of multiple minerals, Miner. Eng. 15 (12) (2002) 1131–1139.

[26] T. Phoo-ngernkham, S. Hanjitsuwan, N. Damrongwiriyanupap, P. Chindaprasirt, Effect of sodium hydroxide and sodium silicate solutions on strengths of alkali activated high calcium fly ash containing Portland cement, KSCE J. Civ. Eng. 21 (6) (2017) 2202–2210.

[27] T. Phoo-ngernkham, A. Maegawa, N. Mishima, S. Hatanaka, P. Chindaprasirt, Effects of sodium hydroxide and sodium silicate solutions on compressive and shear bond strengths of FA–GBFS geopolymer, Constr. Build. Mater. 91 (2015) 1–8.

[28] T. Phoo-ngernkham, S. Hanjitsuwan, C. Suksiripattanapong, J. Thumrongvut, J. Suebsuk, S. Sookasem, Flexural strength of notched concrete beam filled with alkali-activated binders under different types of alkali solutions, Constr. Build. Mater. 127 (2016) 673–678.

[29] C. Ferone, F. Colangelo, R. Cioffi, F. Montagnaro, L. Santoro, Mechanical performances of weathered coal fly ash based geopolymer bricks, Procedia Eng. 21 (2011) 745–752.

[30] M.C. Bignozzi, S. Manzi, M.E. Natali, W.D. Rickard, A. Van Riessen, Room temperature alkali activation of fly ash: the effect of Na2O/SiO2 ratio, Constr. Build. Mater. 69 (2014) 262–270.

[31] M. Criado, A. Fernández-Jiménez, A. De La Torre, M. Aranda, A. Palomo, An XRD study of the effect of the SiO2/Na2O ratio on the alkali activation of fly ash, Cem. Concr. Res. 37 (5) (2007) 671–679.

[32] M. Criado, A. Fernández-Jiménez, A. Palomo, Alkali activation of fly ash: effect of the SiO2/Na2O ratio: part I: FTIR study, Microporous Mesoporous Mater. 106 (1–3) (2007) 180–191.

[33] D. Hardjito, S.E. Wallah, D.M. Sumajouw, B.V. Rangan, Fly ash-based geopolymer concrete, Aust. J. Struct. Eng. 6 (1) (2005) 77–86.

[34] F. Škvára, L. Kopecký, J. Nemecek, Z. Bittnar, Microstructure of geopolymer materials based on fly ash, Ceramics-Silikaty 50 (4) (2006) 208–215.

[35] K. Somna, C. Jaturapitakkul, P. Kajitvichyanukul, P. Chindaprasirt, NaOH-activated ground fly ash geopolymer cured at ambient temperature, Fuel 90 (6) (2011) 2118–2124.

[36] D. Hardjito, B.V. Rangan, Development and properties of low-calcium fly ash-based geopolymer concrete, Research Report GC-1, 2005.

[37] A.S. De Vargas, D.C. Dal Molin, A.C. Vilela, F.J. Da Silva, B. Pavao, H. Veit, The effects of Na 2 O/SiO 2 molar ratio, curing temperature and age on compressive strength, morphology and microstructure of alkali-activated fly ash-based geopolymers, Cem. Concr. Compos. 33 (6) (2011) 653–660.

[38] W. Lee, J. Van Deventer, The interface between natural siliceous aggregates and geopolymers, Cem. Concr. Res. 34 (2) (2004) 195–206.

[39] P.E. Stutzman, Scanning electron microscopy in concrete petrography, Nat. Inst. Stand. Technol. 2 (2001).

[40] I. Garcia-Lodeiro, A. Palomo, A. Fernández-Jiménez, D. Macphee, Compatibility studies between NASH and CASH gels. Study in the ternary diagram Na 2 O–CaO–Al 2 O 3–SiO 2–H 2 O, Cem. Concr. Res. 41 (9) (2011) 923–931.

[41] V. Šmilauer, F. Škvára, J. Němeček, L. Kopecký, P. Hlaváček, Application of Micromechanics on Alkali-activated Materials. Advances in Science and Technology, Trans Tech Publ, 2010.

[42] D. Hardjito, S.E. Wallah, D.M. Sumajouw, B.V. Rangan, On the development of fly ash-based geopolymer concrete, Mater. J. 101 (6) (2004) 467–472.

[43] T. Bakharev, Geopolymeric materials prepared using Class F fly ash and elevated temperature curing, Cem. Concr. Res. 35 (6) (2005) 1224–1232.

[44] M. Miller, C. Bobko, M. Vandamme, F.-J. Ulm, Surface roughness criteria for cement paste nanoindentation, Cem. Concr. Res. 38 (4) (2008) 467–476.

[45] K. Kjellsen, A. Monsøy, K. Isachsen, R. Detwiler, Preparation of flat-polished specimens for SEM-backscattered electron imaging and X-ray microanalysis—importance of epoxy impregnation, Cem. Concr. Res. 33 (4) (2003) 611–616.

[46] J. Maso, Interfacial Transition Zone in Concrete, CRC Press, 2004.

[47] W.C. Oliver, G.M. Pharr, An improved technique for determining hardness and elastic modulus using load and displacement sensing indentation experiments, J. Mater. Res. 7 (6) (1992) 1564–1583.

[48] J.C. Hay, A. Bolshakov, G. Pharr, A critical examination of the fundamental relations used in the analysis of nanoindentation data, J. Mater. Res. 14 (6) (1999) 2296–2305.

[49] G. Constantinides, K.R. Chandran, F.-J. Ulm, K. Van Vliet, Grid indentation analysis of composite microstructure and mechanics: principles and validation, Mater. Sci. Eng.: A 430 (1–2) (2006) 189–202.

[50] E.W. Washburn, Note on a method of determining the distribution of pore sizes in a porous material, Proc. Natl. Acad. Sci. 7 (4) (1921) 115–116.

[51] S. Das, P. Yang, S.S. Singh, J.C. Mertens, X. Xiao, N. Chawla, N. Neithalath, Effective properties of a fly ash geopolymer: synergistic application of X-ray synchrotron tomography, nanoindentation, and homogenization models, Cem. Concr. Res. 78 (2015) 252–262.

[52] J.L. Provis, J.S.J. Van Deventer, Geopolymers: Structures, Processing, Properties and Industrial Applications, Elsevier, 2009.

[53] F. Škvára, L. Kopecký, V. Šmilauer, Z. Bittnar, Material and structural characterization of alkali activated low-calcium brown coal fly ash, J. Hazard. Mater. 168 (2) (2009) 711–720.

[54] Y. Ma, J. Hu, G. Ye, The pore structure and permeability of alkali activated fly ash, Fuel 104 (2013) 771–780.

[55] J. Němeček, V. Šmilauer, L. Kopecký, in: Characterization of Alkali-activated Fly-ash by Nanoindentation. Nanotechnology in Construction 3, Springer, 2009, pp. 337–343.

[56] S. Lu, E. Landis, D. Keane, X-ray microtomographic studies of pore structure and permeability in Portland cement concrete, Mater. Struct. 39 (6) (2006) 611–620.

[57] J. Zhou, G. Ye, K. Van Breugel, Characterization of pore structure in cement-based materials using pressurization–depressurization cycling mercury intrusion porosimetry (PDC-MIP), Cem. Concr. Res. 40 (7) (2010) 1120–1128.

[58] R.A. Cook, K.C. Hover, Mercury porosimetry of hardened cement pastes, Cem. Concr. Res. 29 (6) (1999) 933–943.

[59] S. Mindess, J. Young, D. Darwin, Concrete; Second Edi., Pearson Education Inc, Upper Saddle River, NJ, 2003.

[60] P. Halamickova, R.J. Detwiler, D.P. Bentz, E.J. Garboczi, Water permeability and chloride ion diffusion in Portland cement mortars: relationship to sand content and critical pore diameter, Cem. Concr. Res. 25 (4) (1995) 790–802.

[61] L.-O. Nilsson, Durability concept; pore structure and transport processes, Adv. Concr. Technol. 2 (2003).

[62] N. Ranjbar, S. Talebian, M. Mehrali, C. Kuenzel, H.S.C. Metselaar, M.Z. Jumaat, Mechanisms of interfacial bond in steel and polypropylene fiber reinforced geopolymer composites, Compos. Sci. Technol. 122 (2016) 73–81.

[63] L. Hong, X. Gu, F. Lin, Influence of aggregate surface roughness on mechanical properties of interface and concrete, Constr. Build. Mater. 65 (2014) 338–349.

[64] S. Caliskan, B.L. Karihaloo, Effect of surface roughness, type and size of model aggregates on the bond strength of aggregate/mortar interface, Interface Sci. 12 (4) (2004) 361–374.

[65] H.F. Haghshenas, Y.-R. Kim, M.D. Morton, T. Smith, M. Khedmati, D.F. Haghshenas, Effect of softening additives on the moisture susceptibility of recycled bituminous materials using chemical-mechanical-imaging methods, J. Mater. Civ. Eng. 30 (9) (2018) 04018207.